minerals

Article

Sericite $^{40}Ar/^{39}Ar$ Dating and Indosinian Mineralization in the Liushuping Au–Zn Deposit, West Qinling Orogen, China

Suwei Yue [1,*], Xiaohua Deng [2,3,*], Xiaoxu Yan [1] and Jianxiang Chen [4]

[1] School of Jewelry, Guangzhou City University of Technology, Guangzhou 510800, China; yanxiaoxu@gcu.edu.cn
[2] School of Earth Science and Resources, Chang'an University, Xi'an 710054, China
[3] Beijing Institute of Geology for Mineral Resources Co., Ltd., Beijing 100012, China
[4] The Hanzhong Geological Team of Shaanxi Geological Exploration Bureau, Hanzhong 723000, China; hanzhongchen777@163.com
* Correspondence: yuesuwei@gcu.edu.cn (S.Y.); dxh198411@126.com (X.D.)

Abstract: The Liushuping deposit, located on the northeast margin of the Bikou Block, is the middle-sized gold-zinc deposit (with ore reserves of 15.67 × 10^4 t Zn and 2.2 t Au) in the Mianxian–Lueyang–Yangpingguan area. The orebodies occur in the meta-dolomite of the Duantouya and Jiudaoguai formations controlled by the Jiudaoguai syncline. The ore-forming process has experienced hydrothermal period and epigenetic oxidation period, and the hydrothermal period can be divided into two stages. The hydrothermal sericite sample collected from stage 2 yielded a well-defined $^{40}Ar/^{39}Ar$ isotopic plateau age of 215.70 ± 0.37 Ma, and an $^{39}Ar/^{36}Ar$-$^{40}Ar/^{36}Ar$ normal isochron age of 215.35 ± 0.38 Ma, indicating that the metallogenic age of the Liushuping is the Late Triassic (ca. 215 Ma). The I_{Sr}(t) of sphalerite is higher than that of the Bikou Group but similar to the Duantouya Formation, indicating that the ore-forming fluids may mainly originate from the metamorphic dehydration of the Duantouya Formation. The Liushuping Au–Zn deposit is consistent with that of the Qinling Indosinian orogeny and mineralization, which are related to oceanic subduction during the Late Triassic.

Keywords: sericite $^{40}Ar/^{39}Ar$ dating; Sr isotopes; Liushuping Au–Zn deposit; West Qinling Orogen

check for updates

Citation: Yue, S.; Deng, X.; Yan, X.; Chen, J. Sericite $^{40}Ar/^{39}Ar$ Dating and Indosinian Mineralization in the Liushuping Au–Zn Deposit, West Qinling Orogen, China. *Minerals* **2022**, *12*, 666. https://doi.org/10.3390/min12060666

Academic Editor: Koen De Jong

Received: 9 April 2022
Accepted: 19 May 2022
Published: 25 May 2022

1. Introduction

The Qinling Orogenic Belt (QOB) is well-endowed with mineral systems in China [1–3] (Figure 1a), including a large number of orogenic deposits formed during the Indosinian period (ca. 220 to 190 Ma) [2–5]. The Mianxian–Lueyang–Yangpingguan area (MLY) is located in the Southwest of the QOB (Figure 1), bounded by the Hanjiang Fault and the Mian-Lue Suture to the south and north, respectively (Figure 1b). The MLY area belongs to the northeast part of the Bikou Terrane and hosts a large number of mineral deposits, i.e., gold, nickel, zinc, and lead, which is known as the "Golden Triangle" [6]. The Liushuping is a gold–zinc deposit discovered in recent years, with proven zinc reserves of 15.67 × 10^4 t and gold reserves of 2.2 t. Previous studies mainly focused on geological characteristics of the deposit [7,8] and stratigraphic division [9]. However, the ore-forming process and its relationship with regional metamorphism and magmatism are ambiguous.

Hydrothermal mica is a common mineral in the gold deposit, and its precise ^{40}Ar-^{39}Ar plateau age can represent the precipitation age of gold [10–15]. Strontium isotope data of ore minerals, especially sulfides, can be used to evaluate the nature and source of the ore-forming fluids [16–25]. In this contribution, we selected hydrothermal sericites from the main stage to restrict the age of the Liushuping gold–zinc deposit. In addition, Sr isotope of sphalerites are used to trace the source of ore-forming fluids.

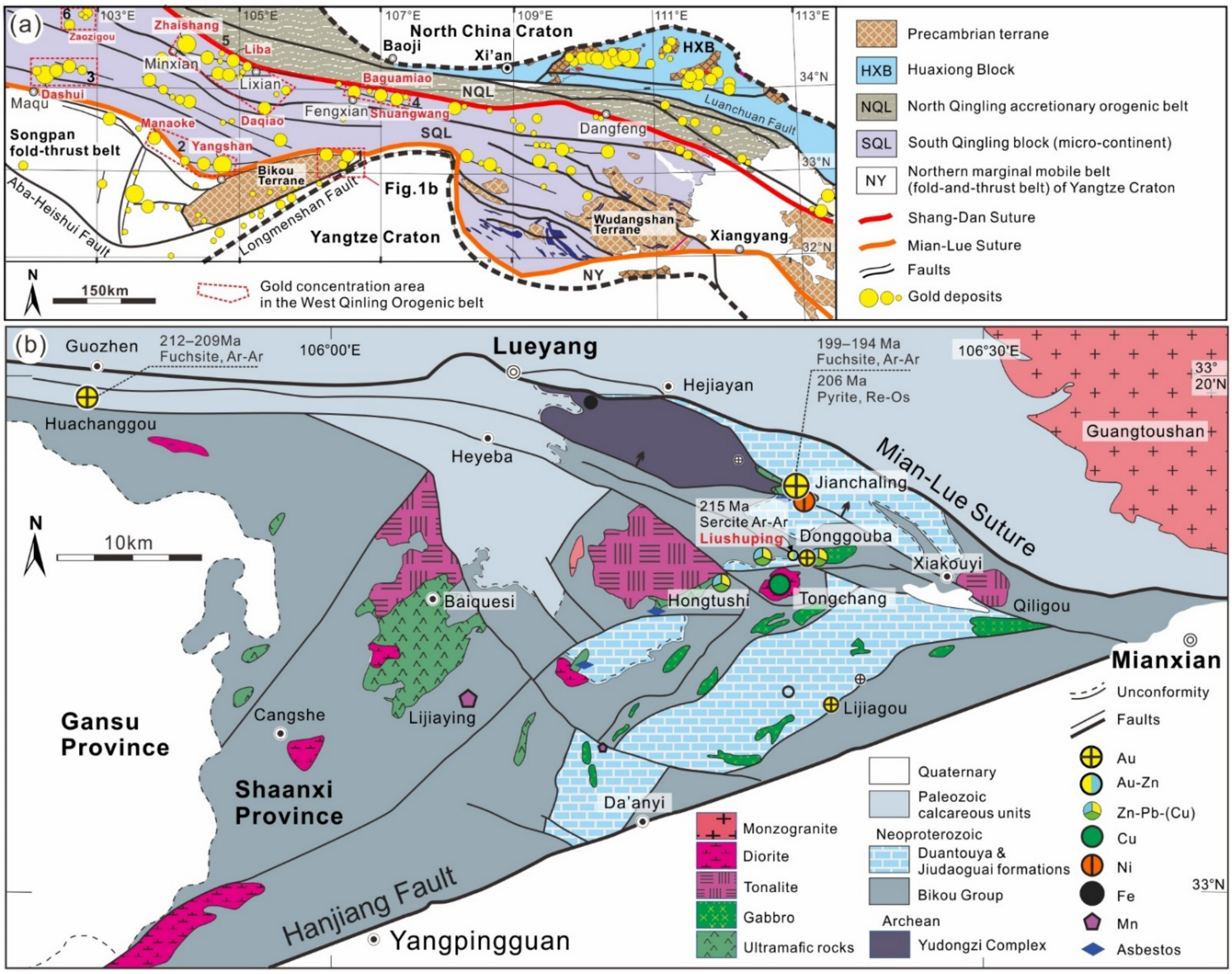

Figure 1. Maps of the: (**a**) tectonic subdivision of the Qinling Orogen, showing the location of the Mianxian–Lueyang–Yangpingguan area (modified after [2]); (**b**) regional geology and location of the Au deposits in the Mianxian–Lueyang–Yangpingguan area, showing the location of the Liushuping Au–Zn deposit (after [6]).

2. Geological Background

2.1. Regional Geology

The outcrop strata in the MLY include the Neoarchean Yudongzi Group (with zircon U-Pb age of 2703 ± 26 Ma and 2661 ± 17 Ma) [26], the Neoproterozoic Bikou Group (zircon U-Pb, 846–776 Ma [27]), the Late Neoproterozoic Duantouya and Jiudaoguai (ca. 651 Ma, whole rock Rb–Sr [28]) formations, and the Paleozoic calcareous units (Figure 1b). These strata have generally experienced low-greenschist to low-amphibolite facies metamorphism [12]. The Bikou Group is the main part of the Bikou Terrane in the northwest corner of the Yangtze Craton (Figure 1a) and is mainly composed of greenschist-facies metamorphosed volcanic–clastic association [29]. The metamorphism of the Duantouya and Jiudaoguai formations is less than the Bikou Group. The NW- and NE-trending ductile-brittle shear zones and brittle faults of the MLY are caused by multiple, variable intense high-pressure deformation and metamorphism. In addition, the distribution of intrusion rocks and mineralization in the area is also controlled by these structures.

2.2. Deposit Geology

The Liushuping Au–Zn deposit is located in the central and eastern part of the MLY, close to the Donggouba Au–Au–(Pb–Zn) deposit (Figure 1b). The strata of the Liushuping ore district are the Bikou Group, Duantouya Formation, and Jiudaoguai Formation, from SW to NE (Figure 2), as well as Devonian metamorphic quartz sandstone and siltstone in the northwest. The Bikou Group comprises quartz–keratophyre and intermediate-acid tuffaceous keratophyre. The Duantouya Formation, unconformably overlying the Bikou Group, is dominated by altered limy dolomite with graphite-bearing mud slate and conglomerate. The Jiudaoguai Formation, conformably overlying the Duantouya Formation, is mainly composed of graphitic silty slate, great thick dolomite, chlorite sericite slate, chlorite sericite slate with carbonate nodules, graphitic silty slate with dolomite lens, thickly layered dolomite with siliceous breccia dolomite, and striped dolomite with thickly layered dolomite lens from bottom to top, which is widespread in the deposit area.

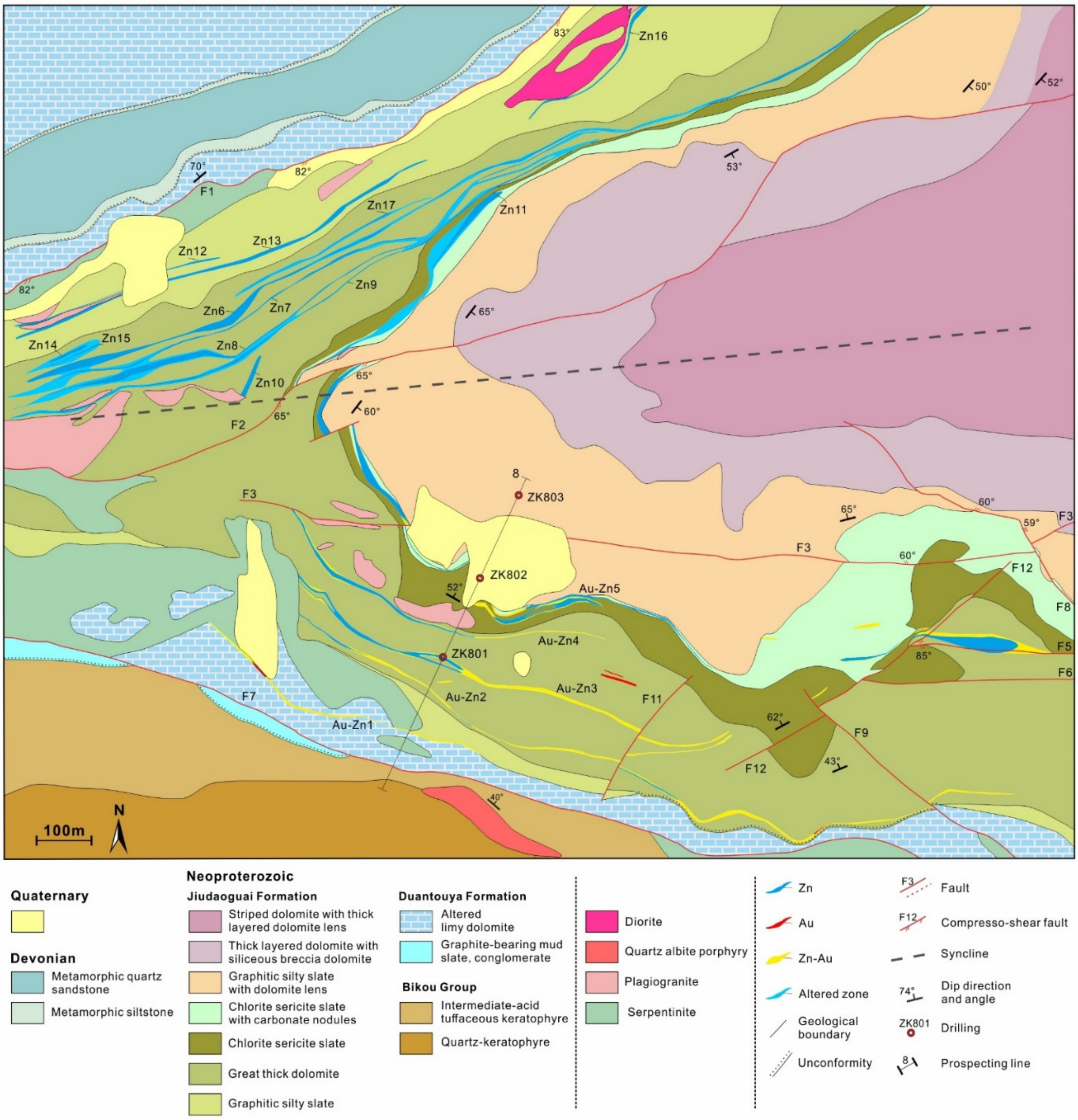

Figure 2. Geological map of the Liushuping Au–Zn deposit.

The magmatic rocks include the quartz albite porphyry exposed in the south of the ore district, diorite in the north, and plagiogranite in the northwest, as well as serpentinized ultrabasic rocks (Figure 2). The fault structure in the ore district can be divided into three groups, nearly EW-, NE-, and NW-trending, respectively. The nearly EW-trending faults are F1, F2, F3, and F7 that penetrate the ore district, and F5 and F6 appear in the eastern part of the ore district. The NE-trending faults F11 and F12 cut through the ore bodies and the strata and are cut by the latest NW-trending faults F8 and F9 (Figure 2).

The Jiudaoguai syncline consists of a set of sedimentary strata, i.e., the Duantouya Formation and the Jiudaoguai Formation unconformable on the volcanic rocks of the Bikou Group (Figure 2). The southern limb strata dip to the NE with a dip angle of 20–45°, and the northern limb strata dip to the SE with a dip angle of 40 to 70°. The Zn–Au ore bodies in the Liushuping occur in the northern and southern limbs of the Jiudaoguai syncline.

The Liushuping deposit consists of two ore prospects: the south ore prospect is located in the southern limb of the Jiudaoguai syncline and contains 5 Au–Zn orebodies, while the north ore prospect is located in the northern limb of the syncline and contains 12 Zn–(Pb) orebodies (Figure 2).

The ore bodies from the south ore prospect have different ore-bearing strata, and their occurrences are relatively consistent (Figure 3). The Au–Zn1 ore body occurs in altered limy dolomite of the Duantouya Formation and is controlled by the interlayer fracture zone. It has a lenticular shape with an average thickness of 0.85 m, with 310° striking and NNW-dipping. The exposed length of the surface is about 300 m, and the average Au grade is 2.45 g/t. The Au–Zn2, Au–Zn3, and Au–Zn4 ore bodies are produced in the thick dolomite of the Jiudaoguai Formation. The Au–Zn2 ore body is narrow and long, outcrop about 500 m, and more than 900 m together with an alteration zone. It is generally NE-dipping with an inclination angle of 46 to 65°. The east side is cut by F11 and F9. The ore body has the longest extension, and all four boreholes can be seen (Figure 3). The thickness of the single-engineering ore body is 0.78–3.47 m, and the average thickness is 3.06 m. The single-engineering gold grade is up to 11.81 g/t, and the average zinc grade is 4.82%. The exposed thickness of the Au–Zn3 ore body is large, extending up to 500 m, and generally contains gold, with a gold grade up to 5.08 g/t. The Au–Zn4 ore body has a relatively small outcrop, about 300 m in length. It can be seen from the borehole with a large thickness of 2.76 m on average. The gold-rich ore bodies are concentrated in the eastern section. the Au–Zn5 ore body occurs in chlorite sericite slate and chlorite sericite slate containing carbonate nodules of the Jiudaoguai Formation. The ore body is dominated by sphalerite with weak gold mineralization, extending about 500 m from east to west (Figure 2).

The orebody of the north ore prospect occurs in the dolomite of the Jiudaoguai Formation on the northern limb of the Jiudaoguai syncline, which is controlled by the interlayer fracture zone. The overall trend of the orebodies is northeast with a dipping southeast and dip angle of 57−67°, which is nearly parallel to the strata in the ore deposit (Figure 2). The length of a single orebody is between 560 m and 1160 m, and the thickness is between 0.48 m and 10.09 m. The orebody generally contains zinc and lead, with average grades of 1.81–3.81% and 0.35–0.36%, respectively.

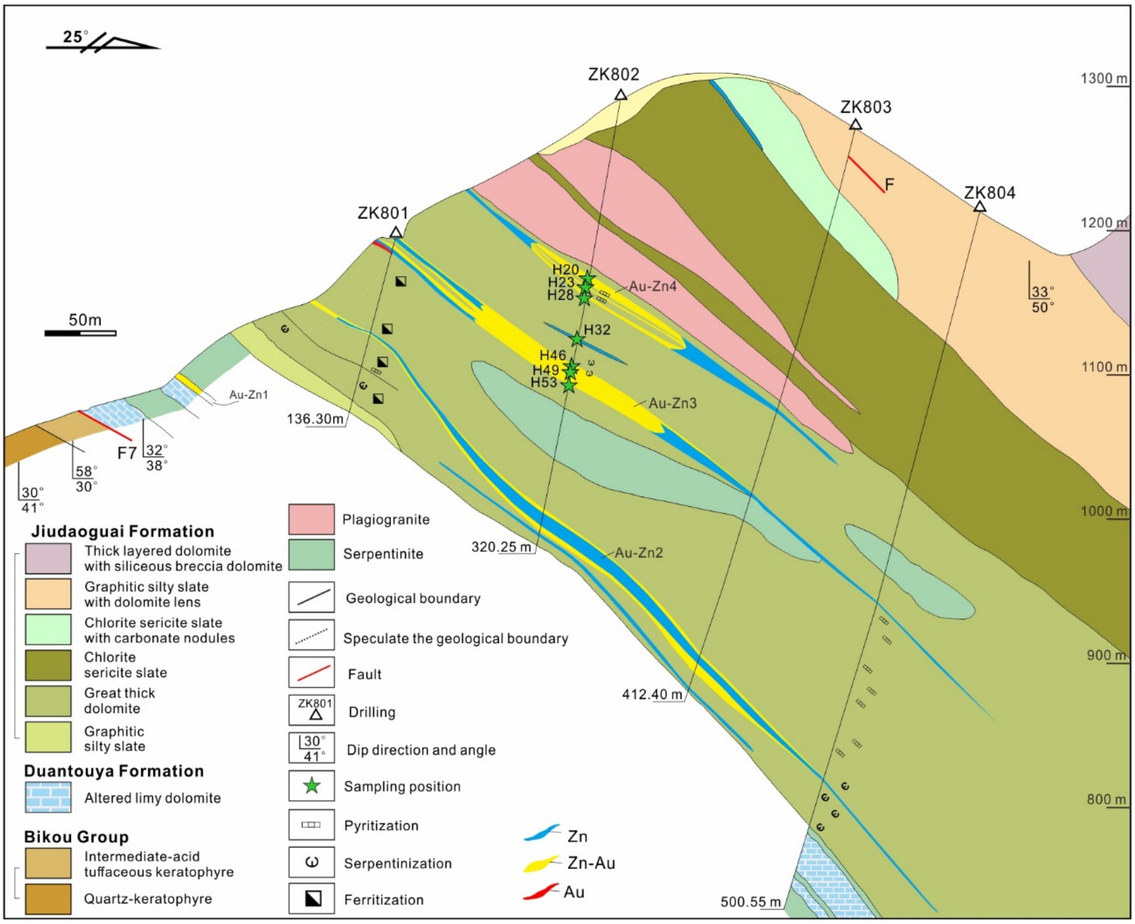

Figure 3. Prospecting line No.8 of the Liushuping Au–Zn deposit.

The ore is mainly pyritized limy dolomite and dolomite, and ferritization is common (Figure 4). The ore contains a massive (Figure 4a,b), vein (Figure 4c), and disseminated structure (Figure 4d,e). The massive ore is dominated by coarse-grained pyrite (Figure 4f,g), interspersed with irregular vein-like sphalerite (Figure 4a,b). In vein-like and disseminated ores, there are few coarse-grained pyrites, and sphalerite–pyrite veins often appear irregular (Figure 4h–j). In the disseminated ores, the sphalerite and transparent minerals are coexistence and present a grid-like feature (Figure 4j), and coarse-grained pyrite is cracked (Figure 4i,j). All ore rocks that are characterized by coarse-grained pyrite are replaced by sphalerite (Figure 4f–h), as well as quartz, calcite, dolomite, sericite, and serpentine (Figure 4l–o).

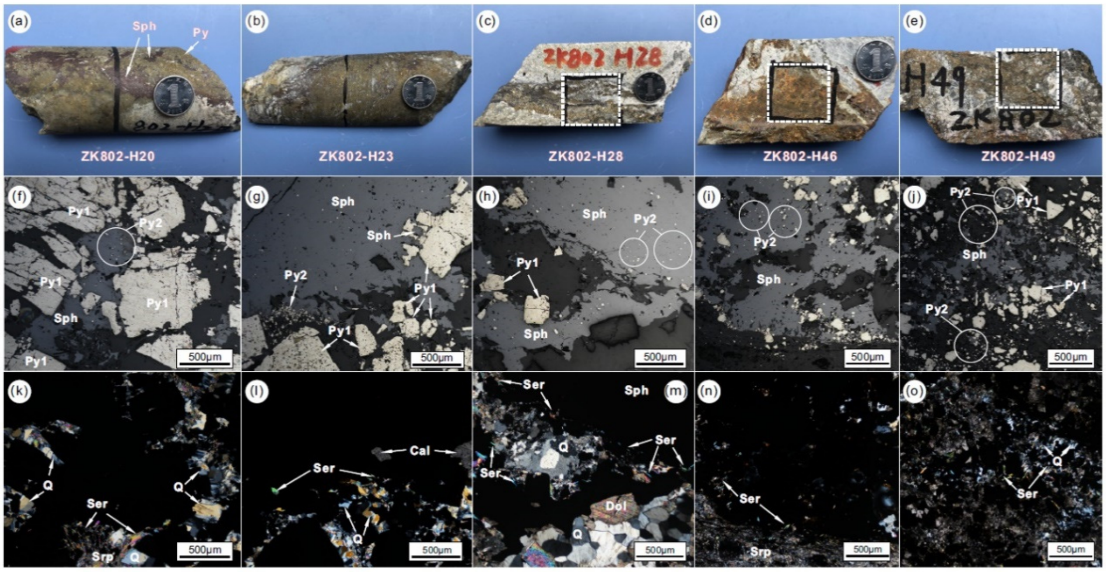

Figure 4. Photographs and photomicrographs showing the ore rocks from drilling ZK801 of the Liushuping Au–Zn deposit: (**a**,**b**) massive structure ore rocks are dominated by coarse-grained pyrites that interspersed with irregular vein-like sphalerite; (**c**) vein structure ore rock; (**d**,**e**) disseminated structure ore rocks, and ferritization; (**f**) coarse-grained pyrites in the massive ore rock; (**g**) coarse-grained pyrites replaced by sphalerite and clustered fine-grained pyrite (Py2) in the massive ore rock; (**h**) the vein-like ores are dominated by sphalerite and clustered fine-grained pyrite (Py2); (**i**,**j**) disseminated ores are dominated by sphalerite and clustered fine-grained pyrite (Py2), coarse-grained pyrites are severely fragmented; (**k**) coexistence of quartz, sericite, calcite, and sphalerite to replace coarse-grained pyrites (Py1), the same position as photo (**f**) under orthogonal polarization; (**l**) coexistence of quartz, sericite, calcite, and sphalerite to replace coarse-grained pyrites (Py1), the same position as photo (**g**) under orthogonal polarization; (**m**) coexistence of quartz, sericite, dolomite, and sphalerite to replace coarse-grained pyrites (Py1), the same position as photo (**h**) under orthogonal polarization; (**n**) coexistence of quartz, sericite, serpentine, and sphalerite, the same position as photo (**i**) under orthogonal polarization; (**o**) coexistence of quartz, sericite, serpentine, carbonates, and sphalerite in the disseminated ore, the same position as photo (**j**) under orthogonal polarization. Abbreviations: Cal—Calcite; Dol—Dolomite; Py—pyrite; Q—quartz; Ser—sericite; Srp—Serpentine; Sph—sphalerite.

According to the petrographic and mineralographic observations, two types of pyrite can be distinguished, i.e., coarse-grained pyrite (Py1) and fine-grained pyrite (Py2). Coarse-grained pyrites (Py1) are generally developed in massive ore (Figure 5b), usually showing fragmented texture (Figure 5b) and replacement texture (Figures 4f,g and 5d). Fine-grained pyrites (Py2) are euhedral or subhedral and often appear in clusters (Figure 5c,e,f) closely associated with sphalerite, indicating the products are of the same stage (Figure 5e–g). Fine-grained pyrites (Py2) are more common in vein-like and disseminated ores (Figure 4i,j). Sphalerite and fine-grained pyrite (Py2) replaced coarse-grained pyrite, showing a metasomatic texture and/or metasomatic residual texture (Figure 5f,g). Some ores, especially disseminated ores, show the appearance of ferritization (Figure 4d,e), which is more obvious under the microscope. In addition, the pyrite has weathered into limonite and formed a pseudomorphic pyrite (Figure 5h,i).

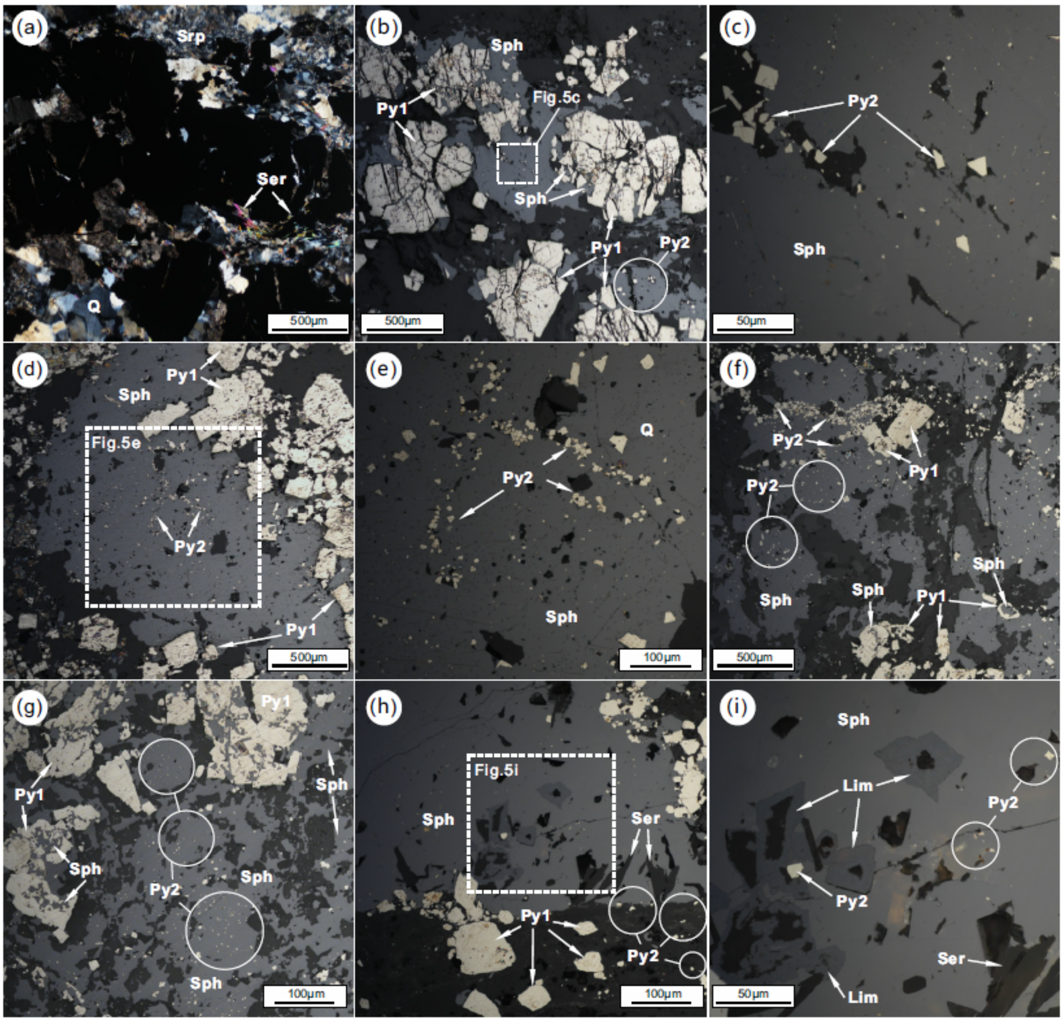

Figure 5. Photomicrographs showing the Liushuping ore petrography: (**a**) coarse-grained pyrite (Py1) replaced by metamorphosed quartz, calcite, dolomite, sericite, serpentine, etc.; (**b**) coarse-grained pyrite (Py1) presents fragmented texture and replaced by sphalerite which coexists with a large amount of fine-grained pyrite (Py2), the same position as photo (**a**); (**c**) coexistence of fine-grained pyrite (Py2) and sphalerite from the stage 2 and exsolution texture between sphalerite and chalcopyrite; (**d**) coarse-grained pyrite (Py1) replaced by sphalerite and fine-grained pyrite (Py2), appearing metasomatic texture; (**e**) fine-grained pyrite (Py2) appearing in clusters with euhedral and subhedral; (**f**) coarse-grained pyrite (Py1) replaced by sphalerite and clustered fine-grained pyrite (Py2), appearing metasomatic texture and metasomatic residual texture; (**g**) partial enlarged detail of photo (**f**); (**h**) limonite presents pseudomorphic pyrite; (**i**) partial enlarged detail of the photo (**h**). Abbreviations: Ccy—Chalcopyrite; Lim—limonite; Py—pyrite; Q—quartz; Ser—sericite; Srp—Serpentine; Sph—sphalerite.

According to the characteristics of ores, as well as the petrographic and mineralographic observations, the deposit is mainly divided into the hydrothermal period and epigenetic oxidation period (Figure 6). The hydrothermal period can be further divided into two stages: stage 1 is mainly composed of coarse-grained pyrite, and stage 2 consists of fine-grained pyrite, sphalerite, quartz, dolomite, calcite, sericite, and serpentine. Limonite is the product of the epigenetic oxidation period.

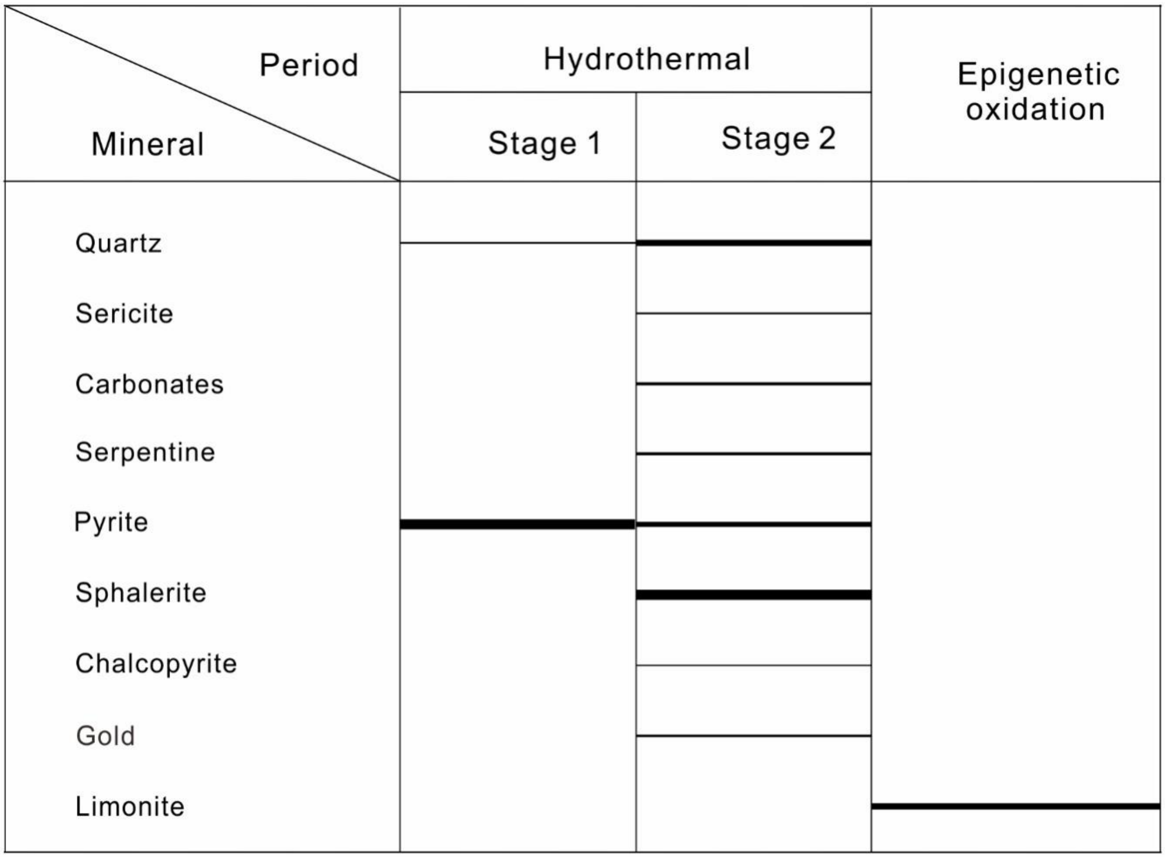

Figure 6. Paragenetic relationship of the minerals at the Liushuping Au–Zn deposit.

3. Sampling and Analytical Methods

3.1. $^{40}Ar/^{39}Ar$ Geochronology

One sample of hydrothermal sericite was collected for ^{40}Ar/^{39}Ar dating (ZK802-H46) from a disseminated ore from the Liushuping drilling ZK802. The samples were crushed into 20 mesh and obtained 0.2 g mica with handpicking under a binocular microscope. The mica was disaggregated, and fragments with no porphyroblasts were reserved. The mica separates for ^{40}Ar/^{39}Ar dating were preliminarily purified from the fragments through a conventional heavy liquid, magnetic technique, and ultrasonic cleaning.

The ^{40}Ar/^{39}Ar analyses were performed at the Western Australian Argon Isotope Facility at Curtin University, Australia. The sample was step-heated using a 110 W Spectron Laser Systems, with a continuous Nd-YAG (IR; 1064 nm) laser rastered over the sample for 1 min to ensure a homogenously distributed temperature. The gas was purified in a stainless-steel extraction line using two SAES AP10 getters, a GP50 getter, and a liquid nitrogen condensation trap. Ar isotopes were measured in static mode using a MAP 215-50 mass spectrometer (resolution of ~500; sensitivity of 4×10^{-14} mol/V) with a Balzers SEV 217 electron multiplier mostly using 9 to 10 cycles of peak-hopping. The data acquisition was performed with the Argus program written by M.O. McWilliams and ran under a LabView environment. The raw data were processed using the ArArCALC software (Version 2.5.2, by Anthony Koppers in Oregon State University, Corvallis, OR, USA; http://earthref.org/tools/ararcalc, accessed on 10 May 2022) [30] and the ages have been calculated using the decay constants recommended by [31]. Blanks were monitored every 3 to 4 steps, and typical ^{40}Ar blanks range from 1×10^{-16} to 2×10^{-16} mol. Our criteria for the determination of plateau were as follows: Plateaus must include at least 70% of ^{39}Ar. The plateau should be distributed over a minimum of 3 consecutive steps agreeing at a 95% confidence level and satisfying a probability of fit (P) of at least 0.05. Plateau ages (Table 1 and Figure 7) are given at the 2σ level and are calculated using the mean of all the plateau steps, each weighted by the inverse variance in their analytical error. Miniplateaus are defined similarly except that they include between 50% and 70% of ^{39}Ar. Integrated ages (2σ) were calculated using the total gas released for each Ar isotope. Inverse isochrons include the maximum number of steps with a probability of fit ≥ 0.05. All sources of uncertainties were included in the calculation.

Table 1. ^{40}Ar/^{39}Ar stepwise laser ablation dating results of sericite from the Liushuping Au–Zn deposit.

Incremental Heating		^{36}Ar(a)	^{37}Ar(ca)	^{38}Ar(cl)	^{39}Ar(k)	^{40}Ar(r)	Age ± 2σ (Ma)	^{40}Ar(r) (%)	^{39}Ar(k) (%)	K/Ca ± 2σ
0M67697	2.5%	0.0000385	0.0039036	0.0001424	0.1607798	1.8669641	215.27	±0.30	99.38	77.30
0M67699	3.0%	0.0000047	0.0007704	0.0000187	0.0104344	0.1218713	216.45	±3.40	98.85	5.02
0M67700	3.4%	0.0000045	0.0000117	0.0000000	0.0087171	0.1017693	216.36	±4.02	98.68	4.19
0M67701	3.8%	0.0000043	0.0003129	0.0000000	0.0047127	0.0548295	215.66	±7.39	97.70	2.27
0M67703	4.2%	0.0000017	0.0001409	0.0000000	0.0017017	0.0196322	213.95	±20.74	97.43	0.82
0M67704	4.6%	0.0000014	0.0006985	0.0000116	0.0019322	0.0227152	217.79	±18.03	98.20	0.93
0M67705	5.0%	0.0000054	0.0001915	0.0000286	0.0009990	0.0113136	210.25	±34.98	87.57	0.48
0M67707	5.5%	0.0000062	0.0015218	0.0000069	0.0006195	0.0068257	204.86	±56.50	78.74	0.30
0M67708	6.0%	0.0000093	0.0007242	0.0000119	0.0006258	0.0075472	223.07	±55.33	73.16	0.30
0M67709	6.5%	0.0000151	0.0005116	0.0000000	0.0002997	0.0035882	221.54	±116.51	44.38	0.14
0M67711	7.0%	0.0000185	0.0008419	0.0000000	0.0002294	0.0029980	240.58	±151.85	35.14	0.11
0M67712	8.0%	0.0000311	0.0000332	0.0000166	0.0003255	0.0037955	216.13	±108.81	28.99	0.16
0M67713	10.0%	0.0000747	0.0005468	0.0000152	0.0001985	0.0011488	110.51	±185.36	4.90	0.10
0M67715	15.0%	0.0002189	0.0008156	0.0000000	0.0005482	0.0029633	103.40	±70.91	4.34	0.26
0M67716	20.0%	0.0002823	0.0002758	0.0000210	0.0011638	0.0000955	1.62	±34.68	0.11	0.56
0M67717	25.0%	0.0002357	0.0009840	0.0000047	0.0022553	0.0029179	25.29	±18.29	3.98	1.08
0M67719	35.0%	0.0003918	0.0003067	0.0000313	0.0055102	0.0092863	32.88	±8.05	7.35	2.65
0M67720	45.0%	0.0004254	0.0009277	0.0000000	0.0069444	0.0216853	60.46	±5.40	14.58	3.34

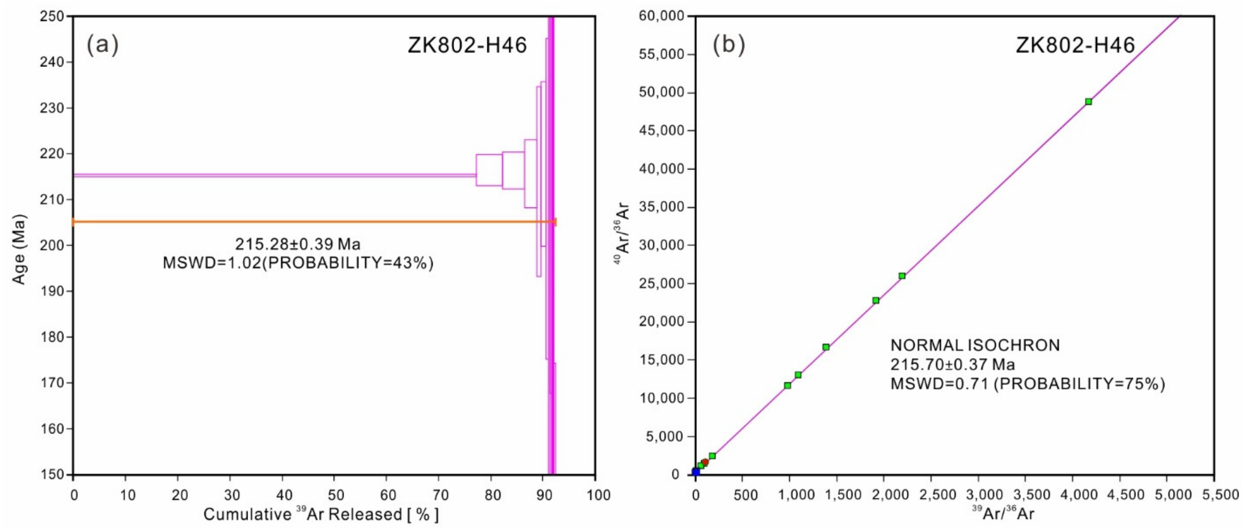

Figure 7. ^{40}Ar/^{39}Ar age speca (**a**) and isochron (**b**) for sericite from the Liushuping Au–Zn deposit.

3.2. Sr Isotope Analysis

Five sphalerite samples were obtained from Stage 2 of the Liushuping Au–Zn deposit, which was crushed into finer than 10 *mesh* (420 microns), and the sulfides were handpicked under a binocular microscope. Around 10 to 50 mg of the powder was leached in acetone and washed with distilled and deionized water to remove contamination, then dried at 60 °C. The samples were then dissolved in a solution of HF + HNO_3 + $HClO_4$, dried, redissolved in 6 N HCl, redried, and redissolved again in 0.5 N HCl (for Sr and Nd separation). The Sr and Nd fractions were separated following the standard chromatographic technique using AG50 × 8 and PTFE–HDEHP resins with HCl as eluent.

A TRITON thermal ionization mass spectrometer (TIMS, Thermo Fisher Scientific, Waltham, Massachusetts, United States) was used to measure the Sr isotopes at the Analytical Laboratory of the Tianjin Institute of Geology and Mineral Resources, China. The $^{87}Sr/^{86}Sr$ isotope ratios were normalized against the $^{86}Sr/^{88}Sr = 0.1194$. The BCR-2 basalt Sr standard was used yielding $^{87}Sr/^{86}Sr$ ratios of 0.705009 ± 0.000008. The Sr isotopic compositions were measured with a thermal ionization ISOPROBE-T mass spectrometer.

4. Results

4.1. Sericite $^{40}Ar/^{39}Ar$ Geochronology

The analytical results are listed in Table 1, and the corresponding plateau age and normal age are plotted in Figure 7. The $^{40}Ar/^{39}Ar$ plateau age of the spectra is defined by: (1) at least 10 contiguous steps of all the gas evolved from the sample and (2) their apparent ages in agreement with the integrated age of the plateau segment with invariability at the 2σ level of uncertainty. The temperatures at which sericite sample ZK802-H46 was measured ranged from 850° to 1400 °C, corresponding to 18 steps of heating released (Figure 7; Table 1. Sample ZK802-H46 has an $^{40}Ar/^{39}Ar$ plateau age of 215.28 ± 0.39 Ma (MSWD = 1.02) at the 1st to 14th heating stages with 92.37% released gas. The corresponding normal isochrones are 215.70 ± 0.37 Ma (MSWD = 0.71) with an initial $^{40}Ar/^{36}Ar$ value of 282.11 ± 8.68, and the inverse isochron is 215.35 ± 0.38 Ma (MSWD = 0.22) with an initial $^{40}Ar/^{36}Ar$ value of 283.85 ± 8.69.

4.2. Sr Isotopes of Sphalerite

The five sphalerite samples (stage 2) yield $^{87}Sr/^{86}Sr$ values of 0.728131–0.755716 (average 0.739492; Table 2) and calculated $I_{Sr}(t)$ values of 0.707447–0.752802 (average 0.730952; Table 2). To conduct a macro-comparison and analysis, we also summarized the Sr data from previous literature and listed it in Table 2.

Table 2. The Sr isotope ratios of sphalerite from the Liushuping Au–Zn deposit and wallrocks from the Bikou block.

Samples No.	Location	Sample	Rb (ppm)	Sr (ppm)	$^{87}Rb/^{86}Sr$	$^{87}Sr/^{86}Sr$	2σ	I_{Sr} (215 Ma)	Ref.
		Duantouya Formation in Jianchaling Au deposit							
PX406-Y-43W	Jianchaling deposit	Dolomite	1.69	108.0000	0.0453	0.719000		0.718861	[32]
G-E-1	Jianchaling deposit	Serpentinized dolomite	8.98	101.0000	0.2576	0.723300		0.722512	[32]
PD404-43-B	Jianchaling deposit	Altered dolomite	36.2	89.6	1.1696	0.713400		0.709824	[32]
960-28-1	Jianchaling deposit	Dolomite	0.027	17.9000	0.0044	0.720582		0.720569	[33]
Zh-5	Jianchaling deposit	Slate	78.4	12.6	18.2861	0.868400		0.812487	[32]
H4	Jianchaling deposit	Slate	105	57.2000	5.3249	0.734027		0.717745	[33]
Average		**N = 6**				**0.746452**		**0.733666**	
		Bikou Group							
2000224	Nanfanba-Mianwanli	Andesitic basalt	19.554	594.5870	0.0951	0.704471	0.000020	0.704180	[34]
2000225	Nanfanba-Mianwanli	Andesite	5.329	118.5830	0.1300	0.704899	0.000020	0.704502	[34]
2000226	Nanfanba-Mianwanli	Basalt	3.948	41.5780	0.2746	0.703211	0.000020	0.702371	[34]
2000228	Nanfanba-Mianwanli	Basalt	3.871	18.1520	0.6168	0.703534	0.000036	0.701648	[34]
2000230	Nanfanba-Mianwanli	Basalt	3.734	39.6950	0.2720	0.702650	0.000020	0.701818	[34]
2000231	Nanfanba-Mianwanli	Basalt	23.01	243.9600	0.2730	0.713325	0.000017	0.712490	[34]
BKL-19		Metamorphosed basalt	23.4	563	0.1203	0.710419	0.000024	0.710051	[35]
BKL-01		Metamorphosed basalt	0.21	111	0.0055	0.707353	0.000022	0.707336	[35]
BKL-06		Metamorphosed basalt	0.13	143	0.0026	0.706668	0.000028	0.706660	[35]
87-104	Hongyangou	Basic lavas	6.464	287.2860	0.0651	0.706763	0.000078	0.706564	[36]
93-17	Hongyangou	Basic lavas	5.288	262.266	0.0583	0.705434	0.000085	0.705256	[36]
87-88	Xintianba-Heimulin	Basic lavas	14.55	138.8	0.3033	0.709308	0.000014	0.708380	[36]
93-55	Xintianba-Heimulin	Basic lavas	6.65	387.9	0.0496	0.706277	0.000012	0.706125	[36]
94-7-1	Xintianba-Heimulin	Basic lavas	9.11	594.94	0.0443	0.708368	0.000026	0.708233	[36]
94-7-2	Xintianba-Heimulin	Basic lavas	9.71	583.5	0.0482	0.708387	0.000061	0.708240	[36]
94-9	Xintianba-Heimulin	Basic lavas	27.6	351.75	0.2270	0.709297	0.000088	0.708603	[36]
94-10	Xintianba-Heimulin	Basic lavas	8.19	171.75	0.1380	0.708812	0.000049	0.708390	[36]
225	Baiyang-Bikou	Basic lavas	1.777	112.9	0.0455	0.704899	0.000020	0.704760	[36]
231	Baiyang-Bikou	Basic lavas	19.45	237.2	0.2374	0.713325	0.000017	0.712599	[36]
Average		**N = 19**				**0.707232**		**0.706748**	

Table 2. *Cont.*

Samples No.	Location	Sample	Rb (ppm)	Sr (ppm)	$^{87}Rb/^{86}Sr$	$^{87}Sr/^{86}Sr$	2σ	I_{Sr} (215 Ma)	Ref.
		Sphalerite in Liushuping Au–Zn deposit							
ZK802-20	Liushuping deposit	Sphalerite	0.2056	0.6272	0.9529	0.755716	0.000008	0.752802	This study
ZK802-23	Liushuping deposit	Sphalerite	0.6004	0.6125	2.8471	0.747161	0.000010	0.738455	This study
ZK802-28	Liushuping deposit	Sphalerite	0.1518	0.7607	0.5789	0.734831	0.000008	0.733061	This study
ZK802-46	Liushuping deposit	Sphalerite	0.4361	0.7524	1.68037	0.728131	0.000010	0.722993	This study
ZK802-62	Liushuping deposit	Sphalerite	2.2870	0.8390	7.90534	0.731619	0.000008	0.707447	This study
Average		**N = 5**				**0.739492**		**0.730952**	

5. Discussion

5.1. Timing of Au–Zn Deposit Formation

One sericite sample from Liushuping yielded an $^{40}Ar/^{39}Ar$ isotopic plateau age of 215.28 ± 0.39 Ma, correlating with an $^{39}Ar/^{36}Ar$-$^{40}Ar/^{36}Ar$ normal isochron age of 215.70 ± 0.37 Ma. The initial $^{40}Ar/^{36}Ar$ values of the sericites are almost consistent with the atmospheric value of 298.56 ± 0.31 [37] within analytical error, indicating the $^{40}Ar/^{36}Ar$ age of the sample to be reliable. The coincident plateau ages and normal isochrones ages can represent the actual metallogenic ages after systematic error corrections. The micro-petrographic study indicates the coexistence of sericites and sphalerite (Figure 8a–c); hence, the age of sericite can represent the sphalerite mineralization. We thus conclude that the sphalerite mineralization with a small amount of gold in the Liushuping deposit occurred in Late Indosinian, which is consistent with the age of the Huachanggou Au deposit in the MLY (212–209 Ma [10]; Figure 1b).

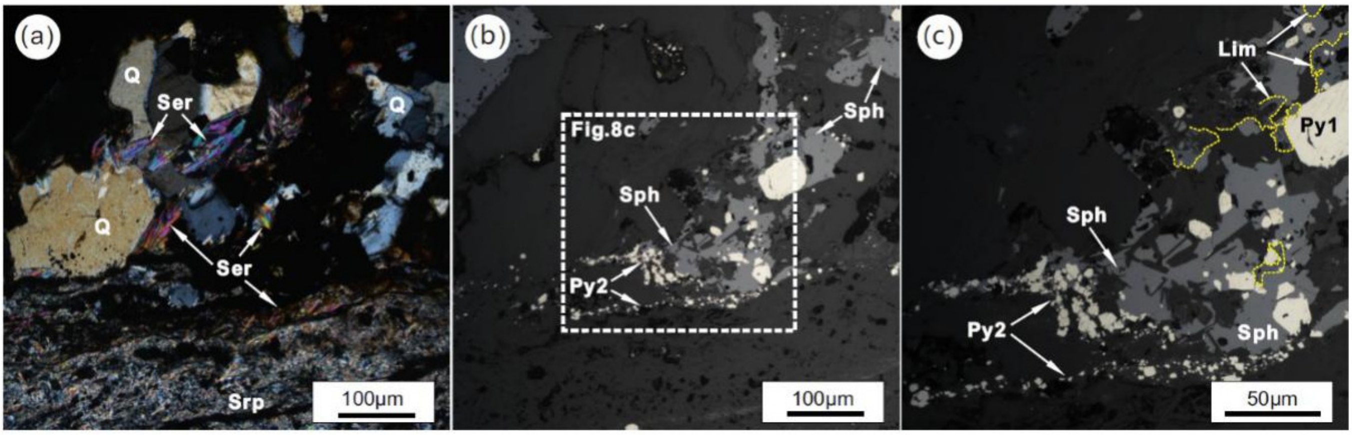

Figure 8. Paragenetic relationship between sphalerite and sericite at the Liushuping Au–Zn deposit. (**a**) coexistence of sericite, quartz, and serpentine in stage 2, under orthogonal polarization; (**b**) coexistence of sericite, sphalerite, and fine-grained pyrite (Py2) to replace coarse-grained pyrites (Py1), the same position as photo (**a**); (**c**) coexistence of sericite and sphalerite, partial enlargement of (**b**). Abbreviations: Lim—limonite; Py—pyrite; Q—quartz; Ser—sericite; Srp—Serpentine; Sph—sphalerite.

5.2. Source of Ore-Forming Materials

As known, hydrothermal deposits are products of water–rock reactions between ore-forming fluids and wall rocks. Therefore, the isotopic composition of wall rocks and ore-forming fluids can be reflected by the isotopic composition of ore minerals [21,38]. In other words, we can infer the isotope compositions of the ore-forming fluids based on the isotope compositions of the unaltered wall rocks and the ores [23], and it has been widely used [18,23,24,39,40].

The sphalerite I_{Sr}(t) values of the Liushuping deposit (0.707447 to 0.752803 Table 2; Figure 9) varies greatly, overlapping with host rocks of the Duantouya Formation (Figure 9). The average I_{Sr}(t) value of sphalerite (0.730952) is much higher than the highest value of the Bikou Group (Figure 9), and close to the counterpart of the Duantouya Formation (0.733668), indicating that the ore-forming fluids mainly originate from sedimentary strata of the Duantouya Formation. Considering that the Jiudaoguai Formation contains Rb-rich carbonatite, even if there is no I_{Sr}(t) data, we proposed the wall rocks of the Jiudaoguai Formation can also provide a high I_{Sr}(t) source. Therefore, the ore-forming fluids may mainly come from the metamorphic fluids derived from the dehydration of the high Sr isotopes strata.

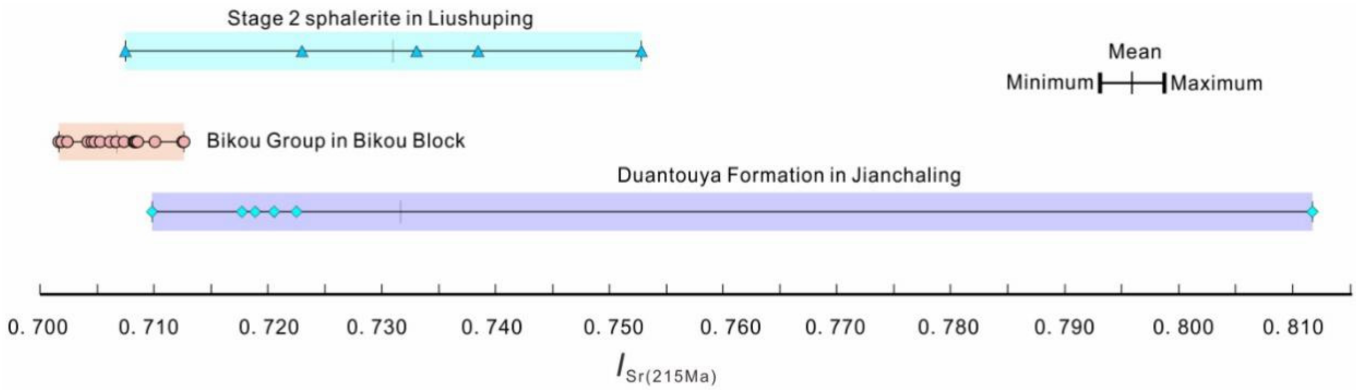

Figure 9. Isotope systematics for the Liushuping deposit showing I_{Sr}(t) plot. t = 215 Ma.

5.3. Geodynamic Setting of Au–Zn Mineralization

The West Qinling Orogenic belt (WQO) was known as the third-largest gold province in China containing more than 50 gold deposits with total gold resources up to 1100 tons [41], which also contained a large amount of copper, lead, and zinc resources. The available metallogenic ages for gold deposits in WQO are listed in Table 3. The predecessors divided the WQO into the southern gold belt and northern gold belt [42]. The former was distributed along the Mianlue suture zone from east to west, including the Mianlueyang, Yangshan–Maonaoke, and Dashui deposits (Figure 1a). The latter was located in the south of the Shangdang suture zone and is composed of Fengxian–Taibai, Daqiao–Liba-Zhaishang, and Zaozigou deposits from the east to west (Figure 1a). Throughout the WQO, two gold metallogenic events in Indosinian and Yanshanian had been identified. The former was from the end of the Triassic to the Early Jurassic (ca. 220 to 190 Ma), and the latter was from the end of the Jurassic to the Early Cretaceous (ca. 150 to 130 Ma) (Table 3; Figure 10). The Yanshanian gold metallogenic event was consistent with the metallogenic ages of gold deposits in the East Qinling, and the metallogenic peak was 135 Ma [43,44], which was interpreted as the interaction between Eurasia and the Pacific plate [43] or to be related to the far-field effect of plate reorganization during the Paleo-Pacific subduction in eastern Eurasia [45].

Table 3. Available age of gold deposits from West Qinling Orogen [42].

No.	Location	Deposit	Type	Metal	Reserves (t)	Analytical Methods	Mineralization Ages (Ma)				Ref.
							Plateau	Isochron	Integrate	Others	
1	Mian-Lue-Yang area	Jianchaling	Orogenic	Au	52	Fuchsite $^{40}Ar/^{39}Ar$	194.32 ± 2.41	198.90 ± 1.98			[12]
						Fuchsite $^{40}Ar/^{39}Ar$	197.30 ± 1.99	198.21 ± 2.40			
						Pyrite Re-Os		206.3 ± 2.7			[42]
						Fuchsite K-Ar				144.2 ± 14.9	[46]
		Huachanggou	Orogenic	Au	35	Fuchsite $^{40}Ar/^{39}Ar$	209.4 ± 2.3	211.4 ± 3.6			[11]
						Fuchsite $^{40}Ar/^{39}Ar$	211.5 ± 2.5	215.3 ± 3.9			
		Liushuping		Au–Zn	2.2	Sericite $^{40}Ar/^{39}Ar$	215.28 ± 0.39	215.7 ± 0.37			This study
2	Yangshan–Manaoke area	Yang shan	Carlin-like	Au	>300	Monazite EPMA U-Th-Pb			190 ± 3		[47]
						Zircon SHRIMP U-Pb				200.9–195.4 137.0–121.4	[48]
						Quartz $^{40}Ar/^{39}Ar$	195.40 ± 1.05	190.75 ± 2.36			[49]
		Manaoke	Carlin	Au	40	Fluid inclusions Rb-Sr		210 ± 35			[50]
3	Dashui area	Dashui	Carlin-like	Au	>150	Calcite Sm-Nd		189.4 ± 1.4			[51]
4	Fengxian–Taibai area	Shuangwang	Orogenic	Au	>70	K-feldspar $^{40}Ar/^{39}Ar$	202.0–198.3				[52]
		Simaoling	Orogenic	Au		Sericite $^{40}Ar/^{39}Ar$	211.9 ± 1.5				[53]
		Baguamiao	Orogenic	Au	106	Calcite and ankerite Sm-Nd		209.3 ± 4.2			
						Muscovite	209.5 ± 1.4				[54]
						Dolomite and ankerite Sm-Nd		208.1 ± 3.1			
						Pyrite U-Th-Pb				210	
						Sericite K-Ar				199.1 ± 4.2	[55]
						Sericite K-Ar				194.4 ± 4.2	
						Quartz $^{40}Ar/^{39}Ar$	131.91 ± 0.89	129.45 ± 0.35			[56]
						Quartz $^{40}Ar/^{39}Ar$	232.58 ± 1.59	222.14 ± 3.45			[57]
		Chaima	Orogenic	Au		Calcite and dolomite Sm-Nd		203.2 ± 1.6			[58]
						Sericite $^{40}Ar/^{39}Ar$	219.0 ± 2.0				[52]
						Sphalerite Rb-Sr		210.8 ± 2.4			[59]

Table 3. *Cont.*

No.	Location	Deposit	Type	Metal	Reserves (t)	Analytical Methods	Mineralization Ages (Ma)				Ref.
							Plateau	Isochron	Integrate	Others	
5	Daqiao–Liba-Zhaishang area	Xiaogouli	Carlin	Au	15	Quartz ^{40}Ar/^{39}Ar	197.45 $\pm$ 1.13	193.24 $\pm$ 0.93			[56]
		Daqiao	Carlin-like	Au	>105	Sericite (aliquots) ^{40}Ar/^{39}Ar	143.2 $\pm$ 2.3		136.2 $\pm$ 3.2		[45]
						Sericite (aliquots) ^{40}Ar/^{39}Ar	143.8 $\pm$ 1.4		139.2 $\pm$ 1.8		
						Sericite (aliquots) ^{40}Ar/^{39}Ar	142.3 $\pm$ 2.5		137.0 $\pm$ 3.6		
						Sericite (aliquots) ^{40}Ar/^{39}Ar	147.9 $\pm$ 0.9		132.2 $\pm$ 2.2		
						Sericite (aliquots) ^{40}Ar/^{39}Ar	150.7 $\pm$ 3.1		146.6 $\pm$ 2.5		
						Sericite (aliquots) ^{40}Ar/^{39}Ar	145.9 $\pm$ 2.5		138.7 $\pm$ 1.8		
						Sericite ^{40}Ar/^{39}Ar	140.1 $\pm$ 0.5		133.1 $\pm$ 1.7		
						Sericite ^{40}Ar/^{39}Ar	130.8 $\pm$ 3.1				
						Sericite (aliquots) ^{40}Ar/^{39}Ar	128.8 $\pm$ 0.6		128.8 $\pm$ 0.6		
						Sericite (aliquots) ^{40}Ar/^{39}Ar	128.6 $\pm$ 0.6		128.5 $\pm$ 0.6		
						Sericite (aliquots) ^{40}Ar/^{39}Ar	127.2 $\pm$ 0.6		128.1 $\pm$ 0.6		
						Sericite (aliquots) ^{40}Ar/^{39}Ar	128.0 $\pm$ 0.6		129.4 $\pm$ 0.6		
		Liba	Carlin-like	Au	80	Quartz ^{40}Ar/^{39}Ar	210.6 $\pm$ 1.26	205.02 $\pm$ 3.53			[60]
						Muscovite and biotite ^{40}Ar/^{39}Ar	216.4 $\pm$ 1.5				[61]
		Zhaishang	Carlin-like	Au	148.7	Quartz ^{40}Ar/^{39}Ar	130.62 $\pm$ 1.38	129.24 $\pm$ 1.23			[62]
						Sericite ^{40}Ar/^{39}Ar	125.28 $\pm$ 1.26	125.56 $\pm$ 1.20			
6	Zaozigou area	Zaozigou	Orogenic	Au-Sb	142	Monazite LA-ICP-MS U-Pb			211.1 $\pm$ 3		[63]
		Ludousou	Orogenic	Au	8	Sericite ^{40}Ar/^{39}Ar	235.68 $\pm$ 0.29	235.61 $\pm$ 0.41			[64]
		Yidinan	Orogenic	Au	>20	Sericite ^{40}Ar/^{39}Ar	220.21 $\pm$ 0.44	220.42 $\pm$ 7.69			[65]

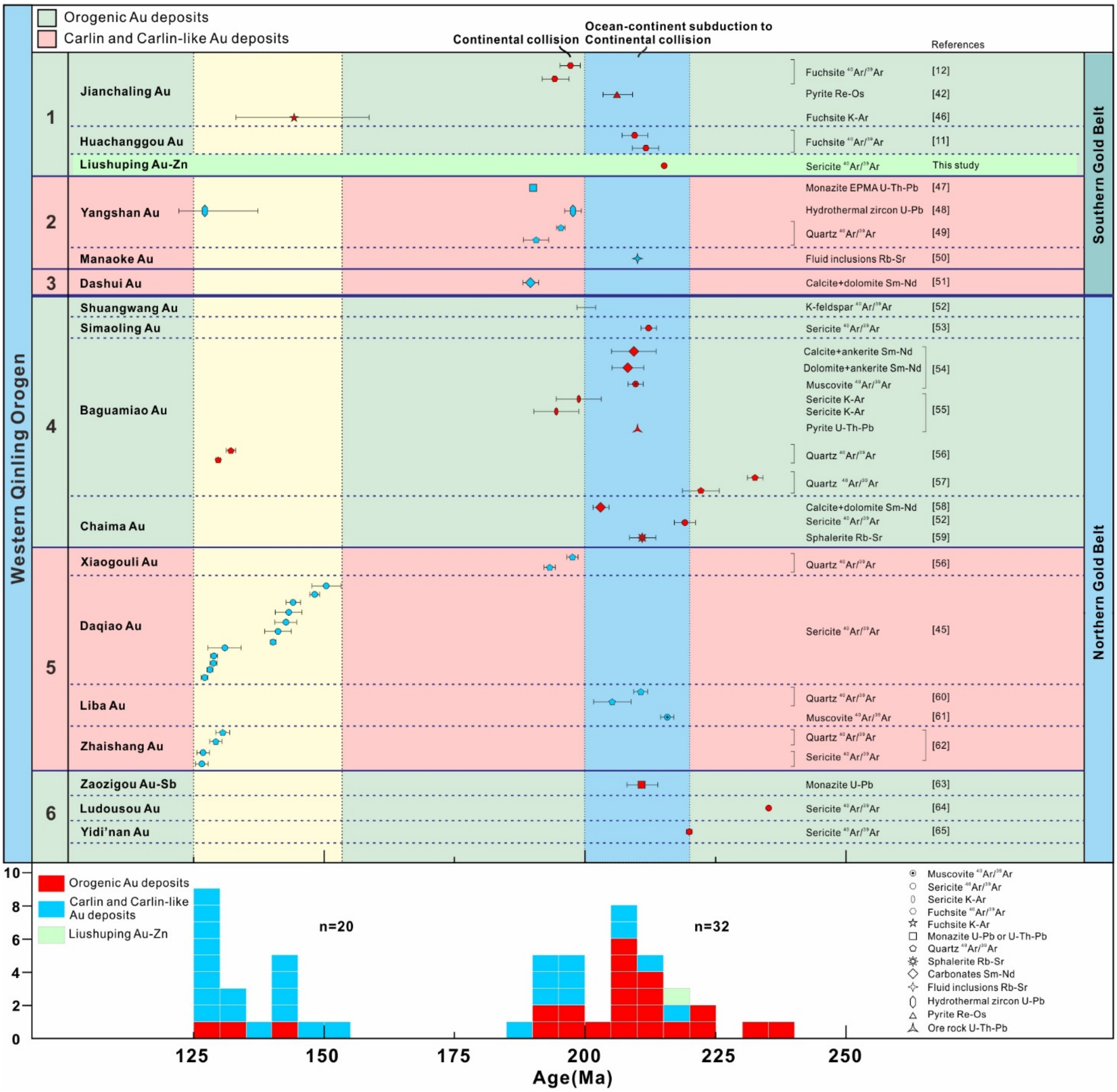

Figure 10. Summary diagram illustrating the ages of Au deposits in the West Qinling Orogen [11,12,42,45–65]. Data sources are listed in Table 3.

The plateau age of the hydrothermal sericite sample obtained in this study is 215.28 ± 0.39 Ma, and the isochronal age is 215.70 ± 0.37 Ma, indicating that the Liushuping Au–Zn deposit was formed in the late Indosinian period. This conclusion coincides with the Indosinian mineralization in the MLY (Figure 1b), such as the Huachanggou Au deposit (fuchsite $^{40}Ar/^{39}Ar$, 212–209 Ma [11]) and the Jianchaling Au deposit (fuchsite $^{40}Ar/^{39}Ar$ 199–194 Ma [12]; pyrite Re-Os 206 Ma [42]). It means that an important metallogenic event occurred in the MLY from the Late Triassic to the Early Jurassic, which coincided with the Indosinian metallogenic of WQO.

Large-scale mineralization that occurred in the WQO in the late Indosinian was closely related to the scissors suture of the Tethys Ocean from east to west. Furthermore, the Triassic Qinling Orogen was analogous to the present-day Mediterranean Sea, contemporaneously accommodating oceanic plate subduction in the west and continental collision in the east, as well as a gradual transition from subduction to collision [2,3]. The onset of the continental collision between the Yangtze and the North China Cratons occurred between 200 and

190 Ma [66]. There are also ore-forming processes in which elements have accumulated to form various kinds of deposits, such as gold, silver, lead, zinc, etc. The metallogenesis of the Huachanggou gold deposit was explained to be related to the collision between the Yangtze terrane and the Qinling microplate, which was further interpreted to have completed the closure of the ocean basin and to have caused the collision between the Yangtze plate and the Qinling microplate before 209 Ma [11]. We also believe that, as the location of the arc point on the northwestern edge of the Yangtze plate, its collision may represent the initial collision between the Yangtze plate and the Qinling microplate [11]. Even at 206 Ma, the formation of the Jianchaling gold deposit still had oceanic subduction, and the mineralization continued until the continental collision in the Early Jurassic [12,42]. Therefore, the Liushuping Au–Zn deposit was formed in ca. 215 Ma, coeval with the end of the oceanic subduction.

6. Conclusions

(1) Two stages of hydrothermal mineralization are recognized in the Liushuping Au–Zn deposit; stage 1 is mainly coarse-grained pyrite, and stage 2 consists of fine-grained pyrite, sphalerite, and gangue minerals.

(2) The sericite from stage 2 yields an $^{40}Ar/^{39}Ar$ plateau age of 215.28 $\pm$ 0.39 Ma (MSWD = 1.02) and a normal isochrone is 215.70 $\pm$ 0.37 Ma (MSWD = 0.71), indicating that the Au–Zn mineralization at Liushuping occurred in the Late Triassic.

(3) The sphalerite I_{Sr}(t) values of the Liushuping deposit (0.707447 to 0.752803) overlapping with host rocks of the Duantouya Formation (0.709824 to 0.812487), but higher than the Bikou Group, which means that ore-forming fluid may mainly originate from the Duantouya Formation.

(4) The Liushuping Au–Zn deposit is the product of metamorphic dehydration of the host rocks, which was formed by the northward subduction of the Yangtze plate under the Qinling microplate during the late Triassic.

Author Contributions: Field geological survey, S.Y., X.Y. and J.C.; writing—original draft, S.Y.; writing—review and editing, X.D. and X.Y.; data analysis, S.Y., X.D. and X.Y. All authors have read and agreed to the published version of the manuscript.

Funding: This study is funded by the National Natural Science Foundation of China (41403032, 41502070 and 41902100). We are grateful to Wen-gang Liu for helping with the isotope analyses and the Hanzhong Geological Team of Shaanxi Geological Exploration Bureau for their field assistance.

Data Availability Statement: Data are available from the authors upon reasonable request.

Conflicts of Interest: The authors declare no conflict of interest.

References

1. Chen, Y.J.; Zhai, M.G.; Jiang, S.Y. Significant Achievements and Open Issues in Study of Orogenesis and Metallogenesis Surrounding the North China Continent. *Acta Petrol. Sin.* **2009**, *25*, 2695–2726.
2. Chen, Y.J. Indosinian Tectonic Setting, Magmatism and Metallogenesis in Qinling Orogen, Central China. *Geol. China* **2010**, *37*, 854–865.
3. Chen, Y.J.; Santosh, M. Triassic Tectonics and Mineral Systems in the Qinling Orogen, Central China. *Geol. J.* **2014**, *49*, 338–358. [CrossRef]
4. Chen, Y.J. Orogenic-Type Deposits and Their Metallogenic Model and Exploration Potential. *Geol. China* **2006**, *33*, 1181–1196.
5. Chen, Y.J. The Development of Continental Collision Metallogeny and Its Application. *Acta Petrol. Sin.* **2013**, *29*, 1–17.
6. Yue, S.W.; Lin, Z.W.; Deng, X.H.; Li, F.R.; He, H.X.; Feng, A.G. C, H, O, S, Pb Isotopic Geochemistry of the Jianchaling Gold Deposit, Shaanxi Province. *Geotecton. Metallog.* **2013**, *37*, 653–670.
7. Chen, J.X.; Wei, Z.D.; Tian, X.A.; Wang, S.X.; Wang, C.C. Mineralization and Geology of the Liushuping Gold Deposit in Lueyang County, Shaanxi Province. *Geol. Shaanxi* **2013**, *31*, 13–19.
8. Chen, J.X.; Yuan, P.; Wang, C.C.; Wei, D.; Tian, X.A.; Liu, Y. The Geological Features and Ore-Controlling Factors of the Liushuping Gold and Zinc Ore Deposits in Lueyang, Shaanxi Province. *J. Geomech.* **2016**, *22*, 212–222.
9. Chen, J.X.; Yuan, P.; Wang, C.C.; Zhao, F.L.; Tian, X.A. Lithostratigraphic Unit Division and Sedimentary Environment Analysis of Nanhua-Sinian System in Liushuping Au–Zn Deposit, Lueyang County, Shaanxi Province. *West-China Explor. Eng.* **2019**, *31*, 167–170.

10. Deng, X.H.; Wang, J.B.; Santosh, M.; Li, Y.C.; Wang, Y.W.; Mao, Q.-G.; Long, L.L.; Chen, X. New $^{40}Ar/^{39}Ar$ Ages from the Kalatag District in the Eastern Tianshan, NW China: Constraints on the Timing of Cu Mineralization and Stratigraphy. *Ore Geol. Rev.* **2018**, *100*, 250–262. [CrossRef]
11. Lin, Z.W.; Zhou, Y.Z.; Qin, Y.; Yue, S.W. Fuchsite $^{40}Ar/^{39}Ar$ Geochronology of the Huachanggou Gold Deposit and Its Tectonic Implications. *Geotecton. Metallog.* **2017**, *41*, 315–324. [CrossRef]
12. Yue, S.W.; Deng, X.H.; Bagas, L.; Lin, Z.W.; Fang, J.; Zhu, C.H.; Zhang, W. Fluid Inclusion Geochemistry and $^{40}Ar/^{39}Ar$ Geochronology Constraints on the Genesis of the Jianchaling Au Deposit, China. *Ore Geol. Rev.* **2017**, *80*, 676–690. [CrossRef]
13. Zheng, Y.; Zhang, L.; Chen, Y.J.; Qin, Y.J.; Liu, C.F. Geology, Fluid Inclusion Geochemistry, and $^{40}Ar/^{39}Ar$ Geochronology of the Wulasigou Cu Deposit, and Their Implications for Ore Genesis, Altay, Xinjiang, China. *Ore Geol. Rev.* **2012**, *49*, 128–140. [CrossRef]
14. Zheng, Y.; Zhang, L.; Li, D.-F.; Kapsiotis, A.; Chen, Y.-J. Genesis of the Dadonggou Pb–Zn Deposit in Kelan Basin, Altay, NW China: Constraints from Zircon U–Pb and Biotite $^{40}Ar/^{39}Ar$ Geochronological Data. *Ore Geol. Rev.* **2015**, *64*, 128–139. [CrossRef]
15. Zheng, Y.; Chen, Y.; Cawood, P.A.; Wang, Y.; Chen, H.; Zhang, L.; Li, D. Late Permian–Triassic Metallogeny in the Chinese Altay Orogen: Constraints from Mica $^{40}Ar/^{39}Ar$ Dating on Ore Deposits. *Gondwana Res.* **2017**, *43*, 4–16. [CrossRef]
16. Jiang, S.Y.; Han, F.; Shen, J.Z.; Palmer, M.R. Chemical and Rb-Sr, Sm-Nd Isotopic Systematics of Tourmaline from the Dachang Sn-Polymetallic Ore Deposit, Guangxi Province, P.R. China. *Chem. Geol.* **1999**, *157*, 49–67. [CrossRef]
17. Kempe, U.; Belyatsky, B.; Krymsky, R.; Kremenetsky, A.; Ivanov, P. Sm-Nd and Sr Isotope Systematics of Scheelite from the Giant Au(-W) Deposit Muruntau (Uzbekistan): Implications for the Age and Sources of Au Mineralization. *Miner. Depos.* **2001**, *36*, 379–392. [CrossRef]
18. Yang, J.H.; Zhou, X.H. Rb-Sr, Sm-Nd, and Pb Isotopes Systematics of Pyrite: Implications for the Age and Genesis of Lode Gold Deposits. *Geology* **2002**, *29*, 711–714. [CrossRef]
19. Chen, Y.J.; Pirajno, F.; Sui, Y.H. Isotope Geochemistry of the Tieluping Silver-Lead Deposit, Henan, China: A Case Study of Orogenic Silver-Dominated Deposits and Related Tectonic Setting. *Miner. Depos.* **2004**, *39*, 560–575. [CrossRef]
20. Barker, S.L.L.; Bennett, V.C.; Cox, S.F.; Norman, M.D.; Gagan, M.K. Sm-Nd, Sr, C and O Isotope Systematics in Hydrothermal Calcite-Fluorite Veins: Implications for Fluid-Rock Reaction and Geochronology. *Chem. Geol.* **2009**, *268*, 58–66. [CrossRef]
21. Pirajno, F. *Hydrothermal Processes and Mineral Systems*; Springer; Geological Survey of Western Australia: Pilbara, Australia, 2009; ISBN 9781402086120.
22. Zhang, L.; Yang, R.S.; Mao, S.D.; Lu, Y.H.; Qin, Y.; Liu, H.J. Sr and Pb Isotopic Feature and Ore-Forming Material Source of the Yangshan Gold Deposit. *Acta Petrol. Sin.* **2009**, *25*, 2811–2822.
23. Ni, Z.Y.; Chen, Y.J.; Li, N.; Zhang, H. Pb–Sr–Nd Isotope Constraints on the Fluid Source of the Dahu Au–Mo Deposit in Qinling Orogen, Central China, and Implication for Triassic Tectonic Setting. *Ore Geol. Rev.* **2012**, *46*, 60–67. [CrossRef]
24. Deng, X.H.; Chen, Y.J.; Santosh, M.; Yao, J.M.; Sun, Y.L. Re–Os and Sr–Nd–Pb Isotope Constraints on Source of Fluids in the Zhifang Mo Deposit, Qinling Orogen, China. *Gondwana Res.* **2016**, *30*, 132–143. [CrossRef]
25. Deng, X.H.; Chen, Y.J.; Santosh, M.; Wang, J.B.; Li, C.; Yue, S.W.; Zheng, Z.; Chen, H.J.; Tang, H.S.; Dong, L.H. U–Pb Zircon, Re–Os Molybdenite Geochronology and Rb–Sr Geochemistry from the Xiaobaishitou W (–Mo) Deposit: Implications for Triassic Tectonic Setting in Eastern Tianshan, NW China. *Ore Geol. Rev.* **2017**, *80*, 332–351. [CrossRef]
26. Zhang, X.; Xu, X.Y.; Song, G.S.; Wang, H.H.; Chen, J.L.; Li, T. Zircon LA-ICP-MS U-Pb Dating and Significance of Yudongzi Group Deformation Granite from Lueyang Area, Western Qinling, China. *Geol. Bull. China* **2010**, *29*, 510–517.
27. Yan, Q.R.; Wang, Z.Q.; Hanson, A.D.; Druschke, P.A.; Yan, Z.; Liu, D.Y.; Jian, P.; Song, B.; Wang, T.; Jiang, C.F. SHRIMP Age and Geochemistry of the Bikou Volcanic Terrane: Implications for Neoproterozoic Tectonics on the Northern Margin of the Yangtze Craton. *Acta Geol. Sin.* **2003**, *77*, 479–490.
28. Qin, K.L.; Yang, J.H. The Age of Phosphorite deposit and Rb-Sr isotopic data in the Hejiayan County, Shannxi Province. *Northwestern Geol.* **1983**, *12*, 43–48.
29. Dong, Y.P.; Santosh, M. Tectonic Architecture and Multiple Orogeny of the Qinling Orogenic Belt, Central China. *Gondwana Res.* **2016**, *29*, 1–40. [CrossRef]
30. Koppers, A.A.P. ArArCALC—Software for $^{40}Ar/^{39}Ar$ Age Calculations. *Comput. Geosci.* **2002**, *28*, 605–619. [CrossRef]
31. Renne, P.R.; Mundil, R.; Balco, G.; Min, K.; Ludwig, K.R. Joint Determination of ^{40}K Decay Constants and $^{40}Ar/^{40}K$ for the Fish Canyon Sanidine Standard, and Improved Accuracy for $^{40}Ar/^{39}Ar$ Geochronology. *Geochim. Cosmochim. Acta* **2010**, *74*, 5349–5367. [CrossRef]
32. Ma, J.Q. *Qinling Orogenic Belt Mianluening Gold Deposit Formation Mode and Prospecting Direction*; Institute of Geochemistry (Guiyang), Chinese Academy of Sciences: Guiyang, China, 1998.
33. Yue, S.W.; Li, D.F.; Bagas, L.; Fang, J.; Lin, Z.W. Geology and Isotope Systematics of the Jianchaling Au Deposit, Shaanxi Province, China: Implications for Mineral Genesis. *Geosciences* **2018**, *8*, 120. [CrossRef]
34. Yan, Q.R.; Andrew, D.H.; Wang, Z.Q.; Yan, Z.; Peter, A.D.; Wang, T.; Liu, D.Y.; Song, B.; Jiang, C.F. Geochemistry and Tectonic Setting of the Bikou Volcanic Terrane on the Northern Margin of the Yangtze Plate. *Acta Petrol. Mineral.* **2004**, *23*, 1–11.
35. Li, Y.F.; Lai, S.C.; Qin, J.F.; Liu, X.; Wang, J. Geochemistry and Sr-Nd-Pb Isotopic Composition of Bikou Group Volcanic Rocks: Evidence of North Yangtze Splitting. *Sci. China Ser. D Earth Sci.* **2007**, *37*, 295–306.
36. Xia, L.Q.; Xia, Z.C.; Xu, X.Y.; Li, X.M.; Ma, Z.P. Petrogenesis of the Bikou Group Volcanic Rocks. *Earth Sci. Front.* **2007**, *14*, 84–101.
37. Lee, J.Y.; Marti, K.; Severinghaus, J.P.; Kawamura, K.; Yoo, H.S.; Lee, J.B.; Kim, J.S. A redetermination of the isotopic abundances of atmospheric Ar. *Geochim. Cosmochim. Acta* **2006**, *70*, 4507–4512. [CrossRef]

38. Chen, Y.J.; Pirajno, F.; Li, N.; Guo, D.S.; Yong, L. Isotope Systematics and Fluid Inclusion Studies of the Qiyugou Breccia Pipe-Hosted Gold Deposit, Qinling Orogen, Henan Province, China: Implications for Ore Genesis. *Ore Geol. Rev.* **2009**, *35*, 245–261. [CrossRef]
39. Chen, Y.J.; Pirajno, F.; Qi, J.P. The Shanggong Gold Deposit, Eastern Qinling Orogen, China: Isotope Geochemistry and Implications for Ore Genesis. *J. Asian Earth Sci.* **2008**, *33*, 252–266. [CrossRef]
40. Chen, Y.J.; Pirajno, F.; Qi, J.P. Origin of Gold Metallogeny and Sources of Ore-Forming Fluids, Jiaodong Province, Eastern China. *Int. Geol. Rev.* **2005**, *47*, 530–549. [CrossRef]
41. Li, N.; Yang, L.Q.; Groves, D.I.; Li, H.X.; Liu, X.W.; Liu, J.; Ye, Y.; Li, H.R.; Liu, C.X.; Yin, C. Tectonic and District to Deposit-Scale Structural Controls on the Ge'erke Orogenic Gold Deposit within the Dashui-Zhongqu District, West Qinling Belt, China. *Ore Geol. Rev.* **2020**, *120*, 103436. [CrossRef]
42. Yue, S.W.; Deng, X.H.; Lin, Z.W. Direct Re–Os Dating of Pyrite from the Jianchaling Au Deposit, West Qinling, China. *Acta Geochim.* **2021**. [CrossRef]
43. Chen, Y.J.; Zhang, J.; Zhang, F.X.; Li, C. Carlin and Carlin-like Gold Deposits in Western Qinling Mountains and Their Metallogenic Time, Tectonic Setting and Model. *Geol. Rev.* **2004**, *50*, 134–152.
44. Chen, Y.J.; Fu, S.G. *Gold Mineralization in West Henan*; Seismological Press: Beijing, China, 1992; ISBN 9787502808013.
45. Wu, Y.F.; Li, J.W.; Evans, K.; Vasconcelos, P.M.; Thiede, D.S.; Fougerouse, D.; Rempel, K. Late Jurassic to Early Cretaceous Age of the Daqiao Gold Deposit, West Qinling Orogen, China: Implications for Regional Metallogeny. *Miner. Depos.* **2018**, *54*, 631–644. [CrossRef]
46. Huang, W.K.; Ran, H.Y. The Metallogenetic Characteristics of Gold Deposits Related to Carbonatized Ultramafites in Ophiolites. *Bull. Mineral. Petrol. Geochem.* **1996**, *15*, 153–156.
47. Yang, R.S.; Chen, Y.J.; Zhang, F.X.; Li, Z.H.; Mao, S.D.; Liu, H.J.; Zhao, C.H. Chemical Th-U-Pb Ages of Monazite from the Yangshan Gold Deposit, Gansu Province and Their Geologic and Metallogenic Implications. *Acta Petrol. Sin.* **2006**, *22*, 2603–2610.
48. Qi, J.Z.; Li, L.; Yuan, S.S.; Liu, Z.J.; Liu, D.Y.; Wang, Y.B.; Li, Z.H. A SHRIMP U-Pb Chronological Study of Zircons from Quartz Veins of Yangshan Gold Deposit, Gansu Province. *Miner. Depos.* **2005**, *24*, 141–150.
49. Qi, J.Z.; Yuan, S.S.; Li, L.; Sun, B.; Guo, J.H.; Li, Z.H.; Fan, Y.X.; Liu, W.; Gao, Q. Bin Geological Features and Ore-Controlling Factors of the Yangshan Superlarge Gold Deposit, Gansu Province, China. *Geol. Rev.* **2003**, *49*, 85–92.
50. Wang, K.Y.; Yao, S.Z.; Yang, Y.C.; Dai, J.Z. Geological Characteristics and Origin of Manaoke Fine-Grained Disseminated Gold Deposit in Northwestern Sichuan Province. *Miner. Depos.* **2004**, *23*, 494–501.
51. Li, L.J.; Li, T.J.; Wang, D. Calcite Sm-Nd Isochron Age of the Dashui Gold Deposit in West Qinling Orogenic Belt and Its Implications. *Geoscience* **2019**, *33*, 469.
52. Liu, X.L.; Wang, Y.T.; Hu, Q.Q.; Wang, R.T.; Peng, L.H.; Zhang, G.L.; Liu, M.; Ouyang, S. Evidence of $^{40}Ar/^{39}Ar$ Age Data for Ore-Forming Time of Chaima Gold Deposit in Fengtai Ore Concentration Area, Shaanxi Province. *Miner. Depos.* **2018**, *37*, 163–174.
53. Wang, Y.T.; Li, X.; WANG, R.T.; Liu, X.L.; Hu, Q.Q.; Li, J.H.; Wang, C.A.; Wen, B.; Wen, S.W.; Wang, S.L. Evidence of Ar-Ar Age for the Metallogenic Epoch of Simaoling Gold Deposit in Fengxian-Taibai Ore Cluster of Shaanxi. *J. Earth Sci. Environ.* **2014**, *36*, 61–69.
54. Wang, Y.T.; Mao, J.W.; Zhang, J.; Wang, R.T.; Chen, G.M.; Hu, Q.Q.; Chen, S.C.; Liu, X.L. Geochronological Constraints on the Baguamiao Gold Deposit, West Qinling Orogen, Central China: Implications for Ore Genesis and Geodynamic Setting. *Ore Geol. Rev.* **2020**, *122*, 103508. [CrossRef]
55. Wei, L.M. *Metallogenic Environment and Prediction for Baguamiao Gold Deposit Type in Qinling Region, China*; Chengdu University of Technology: Chengdu, China, 2004.
56. Shao, S.C.; Wang, D.B. ^{39}Ar-^{40}Ar Dating of the Three Typical Gold Deposits and Its Geological Significance in the Southern Qinling Region. *Acta Geol. Sin.* **2001**, *75*, 106–110.
57. Feng, J.Z.; Shao, S.C.; Wang, D.B.; Wang, X.M.; Ma, Z.G. Baguamiao Superlarge Gold Deposit in the Qinling Orogen: The Characteristics of Its Control by the Brittle–Ductile Shear Zone and Dynamic Mechanism for Ore-Forming Structure. *Geol. China* **2002**, *29*, 58–66.
58. Liu, X.L.; Wang, Y.T.; Hu, Q.Q.; Wei, R.; Wang, R.T.; Wen, S.W.; Chen, M.S.; Yang, G.H. Sm-Nd Isotopic Dating of Carbonate Minerals from the Chaima Gold Deposit in the Fengxian-Taibai Ore Concentration Area, Shaanxi Province and Its Implications. *Acta Petrol. Sin.* **2014**, *30*, 271–280.
59. Wang, Y.T.; Liu, X.L.; Hu, Q.Q.; Zhang, J.; Chen, S.C.; Wang, R.-T.; Dai, J.Z.; Gao, W.H.; Wen, S.W.; Chen, M.S. Rb–Sr Isotopic Dating of Vein-like Sphalerites from the Chaima Au Deposit in Fengxian-Taibai Ore-Concentration Area, Shaanxi Province and Its Geological Significance. *Northwestern Geol.* **2018**, *51*, 121–132.
60. Feng, J.Z.; Wang, D.B.; Wang, X.M.; Shao, S.C.; Lin, G.F.; Shi, J.J. Geology and Metallogenesis of Liba Large-Size Gold Deposit in Lixian, Gansu Province. *Miner. Depos.-Beijing* **2003**, *22*, 257–263.
61. Zeng, Q.T.; McCuaig, T.C.; Hart, C.J.R.; Jourdan, F.; Muhling, J.; Bagas, L. Structural and Geochronological Studies on the Liba Goldfield of the West Qinling Orogen, Central China. *Miner. Depos.* **2012**, *47*, 799–819. [CrossRef]
62. Lu, Y.M.; Li, H.G.; Chen, Y.G.; Zhang, G.L. $^{40}Ar/^{39}Ar$ Dating of Alteration Minerals from Zhaishang Gold Deposit in Minxian County, Gansu Province, and Its Geological Significance. *Miner. Depos.* **2006**, *25*, 590–597.

63. Qiu, K.F.; Yu, H.C.; Deng, J.; McIntire, D.; Gou, Z.Y.; Geng, J.Z.; Chang, Z.S.; Zhu, R.; Li, K.N.; Goldfarb, R. The Giant Zaozigou Au-Sb Deposit in West Qinling, China: Magmatic- or Metamorphic-Hydrothermal Origin? *Miner. Depos.* **2020**, *55*, 345–362. [CrossRef]
64. Yu, H.C.; Qiu, K.F.; Nassif, M.T.; Geng, J.Z.; Sai, S.X.; Duo, D.W.; Huang, Y.Q.; Wang, J. Early Orogenic Gold Mineralization Event in the West Qinling Related to Closure of the Paleo-Tethys Ocean—Constraints from the Ludousou Gold Deposit, Central China. *Ore Geol. Rev.* **2020**, *117*, 103217. [CrossRef]
65. Yu, H.C.; Qiu, K.F.; Sai, S.X.; McIntire, D.C.; Pirajno, F.; Duo, D.W.; Miggins, D.P.; Wang, J.; Jia, R.Y.; Wu, M.Q. Paleo-Tethys Late Triassic Orogenic Gold Mineralization Recorded by the Yidi'nan Gold Deposit, West Qinling, China. *Ore Geol. Rev.* **2020**, *116*, 103211. [CrossRef]
66. Li, N.; Chen, Y.J.; Santosh, M.; Pirajno, F. Compositional Polarity of Triassic Granitoids in the Qinling Orogen, China: Implication for Termination of the Northernmost Paleo-Tethys. *Gondwana Res.* **2015**, *27*, 244–257. [CrossRef]